ACS OMEGA

http://pubs.acs.org/journal/acsodf

Article

One-Pot Synthesis of Hexamethylenetetramine Coupled with H_2 Evolution from Methanol and Ammonia by a Pt/TiO_2 Nanophotocatalyst

Weikun Chen, Xiaoying Liu, Hui Zheng, Xiao Fu, and Youzhu Yuan*

Cite This: *ACS Omega* 2022, 7, 19614−19621

Read Online

ACCESS | Metrics & More | Article Recommendations | Supporting Information

ABSTRACT: Utilization of solar energy for photocatalytic H_2 evolution coupled with value-added chemical synthesis is a promising avenue to address energy and environmental crises. Here, we report the hexamethylenetetramine (HMT) synthesis and H_2 evolution from methanol and ammonia in one pot using a nanophotocatalyst of the conventional semiconductor TiO_2 (P25) loaded with Pt (Pt/P25). The addition of ammonia inhibits byproduct ethylene glycol formation, promotes H_2 evolution, and obtains HMT with high selectivity (>99.0%). The Pt valence state is regulated by calcination and reduction treatment, indicating that Pt/P25 is a stable catalyst for the photocatalytic synthesis of HMT from methanol and ammonia. The optimized formation rates of H_2 and HMT are 71.53 and 11.39 mmol g_{cat}^{-1} h^{-1}, respectively. This work provides a green and sustainable pathway for the photocatalytic HMT synthesis coupled with H_2 evolution under mild conditions.

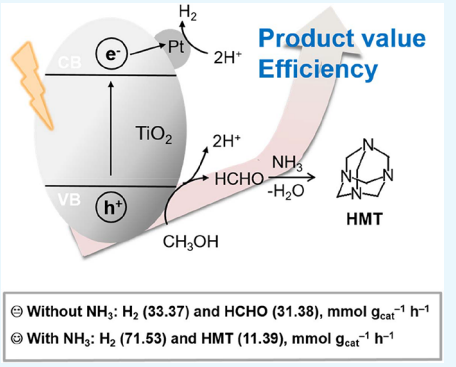

INTRODUCTION

As an important energy source, H_2 evolution by solar-driven water splitting on semiconductor photocatalysts is an environmentally benign, sustainable route, thereby attracting extensive attention.[1,2] In the system of solar-driven H_2 evolution by water splitting, alcohols like methanol, ethanol, and glycerol are commonly added as a sacrificial agent due to the ready recombination of photoexcited electron−hole pairs and the sluggish reaction kinetics.[3−5] The photocatalytic H_2 evolution is markedly accelerated by the consumption of photoexcited holes to suppress the recombination of photoexcited electron−hole pairs in which alcohols can act as a proton donor. In this process, the added alcohols are also oxidized by holes to produce fuel or chemicals, such as H_2, CO, aldehydes, acids, and acetals, of which organic byproducts are often overlooked.[6−8] Therefore, the hole scavengers must be used as feedstock to improve the efficiency of H_2 evolution while conveniently producing high-value chemicals.[9,10] Recently, Chao et al. and Li et al. reported on the tandem anaerobic acetalization of alcohols to the corresponding acetals and H_2 via a photocatalytic process under mild conditions.[11,12] Zhang et al. reported that methanol/ethanol can be converted to the corresponding diols and H_2 by C−C coupling.[13] These studies explored the possibility of combining the evolution of H_2 with the synthesis of fine chemicals in a green and atom-economical way.

Hexamethylenetetramine (HMT), also known as hexamine or urotropine, is a commercially available chemical derived from methanol. HMT has wide industrial applications because it can be used as an industrial raw material, a curing agent of resins, and a vulcanization accelerator of rubber.[14] Moreover, HMT is widely used in organic synthesis and pharmaceutical products because of its unique structure and characteristic of hydrolyzing to formaldehyde and NH_3 under an acidic environment.[15] The industrialized process of HMT production is illustrated in Scheme 1, where methanol is first oxidized and dehydrogenated to form formaldehyde at high temperatures (>300 °C), and then, the as-obtained formaldehyde is transferred to the reactor to react with NH_3.[16] Formaldehyde and NH_3 are mixed in the liquid phase to undergo dehydration

Scheme 1. Two Methodologies for the Synthesis of HMT via Methanol and Ammonia

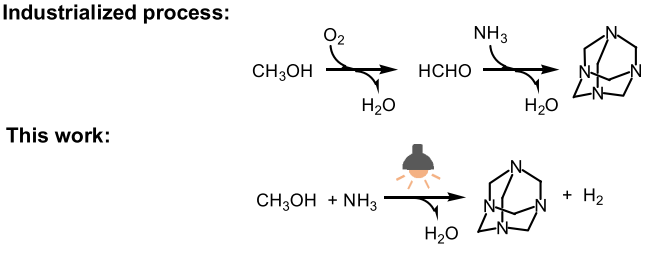

Received: March 5, 2022
Accepted: May 26, 2022
Published: June 6, 2022

and condensation to produce HMT. Nevertheless, the oxidation step for producing formaldehyde has high energy consumption and is complex. Thus, a simple, mild, and economical process is urgently needed.

In this study, we present the conversion of methanol and NH_3 to HMT and H_2 in one pot by using a Pt/TiO_2 nanophotocatalyst under mild conditions. Under light radiation, methanol can undergo dehydrogenation to produce formaldehyde and H_2 on the photocatalyst. NH_3 undergoes a condensation reaction with the dehydrogenation product (formaldehyde) to form HMT, which promotes methanol dehydrogenation (Scheme 1). When the concentration of NH_3 is 1.0 M, the rate of photocatalytic HMT production can reach 11.39 mmol g_{cat}^{-1} h^{-1}, and the H_2 evolution is 71.53 mmol g_{cat}^{-1} h^{-1}. The effect of the valence of Pt on the photocatalytic dehydrogenation activity was also investigated in detail. Thus, a promising method of coupling photocatalytic HMT synthesis and H_2 evolution is proposed.

EXPERIMENTAL SECTION

Catalyst Preparation. Pt, Pd, and Au were loaded onto the P25 support by a photodeposition method according to the procedure in the literature.[17] In the preparation of Pt/P25, 0.1 g of P25 and an appropriate amount of H_2PtCl_6 were added to a 20% methanol aqueous solution, and the Pt content was approximately 0.50 wt %. After stirring for 1 h, the solution was irradiated under a Xe lamp and a N_2 atmosphere for another 1 h. The product was filtered for collection until no Cl^- was detected in the filtrate and dried at 60 °C under vacuum in an oven overnight. The Pt catalysts deposited on commercial anatase and rutile were denoted as Pt/TiO_2-A and Pt/TiO_2-R. To obtain varied valence values of Pt catalysts, Pt/P25 was annealed under different conditions. In brief, Pt/P25 was calcined in air at different temperatures for 3 h, which is denoted as Pt/P25-*x*A (where *x* represents the calcined temperature). The calcined Pt/P25-*x*A was reduced with 5% H_2/Ar at 400 °C for 3 h, which is denoted as Pt/P25-*x*AH.

TiO_2 samples with the (101) and (001) facets were prepared according to the literature.[18] For TiO_2(101), 6.6 mL of $TiCl_4$ was added dropwise into 20.0 mL of HCl aqueous solution (0.4 M) at 0 °C. After stirring for 0.5 h, the solution was added dropwise into 50.0 mL of NH_3 aqueous solution (5.5 wt %) under stirring at room temperature. Then, an appropriate amount of 5.5 wt % NH_3 aqueous solution was added to the above solution to adjust the pH value between 6 and 7. After stirring at room temperature for 2 h, the white precipitate was filtered and washed repeatedly with H_2O until no residual Cl^- could be detected and dried at 70 °C for 12 h to obtain $Ti(OH)_4$. $Ti(OH)_4$ (1.0 g) and 0.1 g of NH_4Cl were dispersed in a mixture of 15.0 mL of ultrapure H_2O and 15.0 mL of isopropyl alcohol under stirring at room temperature, and the mixture was transferred into a 50.0 mL Teflon-lined stainless-steel autoclave and kept at 180 °C for 24 h. The white precipitate obtained was collected by centrifugation and washed with ultrapure H_2O several times. For TiO_2(001), 25.0 mL of $Ti(OBu)_4$ and 3.0 mL of 40 wt % HF aqueous solution were mixed under stirring at room temperature. The suspension was then transferred into a 50.0 mL Teflon-lined stainless-steel autoclave and kept at 180 °C for 24 h. The white precipitate was centrifuged, washed repeatedly with ethanol and ultrapure H_2O, and dried at 80 °C for 12 h. The acquired solid powder was redispersed in 500.0 mL of 0.1 M NaOH aqueous solution and stirred for 24 h at room temperature. The suspension was centrifuged and washed repeatedly with ultrapure H_2O until the pH value of aqueous solution was within 7−8.

Catalyst Characterization. X-ray diffraction analysis was performed using a Rigaku Ultima IV X-ray diffractometer equipped with Cu K_α radiation (40 kV and 30 mA) from 20 to 60° at 10°/min. The actual Pt loading in the catalyst was determined by inductively coupled plasma−mass spectrometry (ICP−MS) on an Agilent ICP-MS 4500 instrument. N_2 physisorption was conducted using a Micromeritics TriStar II 3020, and the specific surfaces of the catalysts were calculated using the Brunauer−Emmett−Teller method. High-angle annular dark-field imaging−scanning transmission electron microscopy (HAADF−STEM) was performed on a Philips Analytical FEI TECNAI F20 electron microscope with a 200 kV electron acceleration voltage. The Pt particle size distribution of approximately 150 individual particles was measured. X-ray photoelectron spectroscopy (XPS) was performed using a PHI QUANTUM 2000 Scanning ESCA Microprobe instrument with an Al K_α radiation source ($h\nu$ = 1486.6 eV) and a binding energy referenced to C 1s (284.6 eV). Ultraviolet−visible (UV−vis) spectroscopic measurements were taken on a Varian Cary 5000 spectrophotometer equipped with a diffuse reflectance accessory. The spectra were collected with $BaSO_4$ as a reference. Electron spin resonance (ESR) spectroscopy was performed on the samples at room temperature using a Bruker EMX-10/12 ESR spectrometer operating at the X-band frequency, and 5,5-dimethyl-1-pyrroline-*N*-oxide (DMPO) was used as the paramagnetic species spin-trap agent. For in situ ESR measurements, 0.35 mL of ammonia aqueous solution was added to 4.65 mL of methanol and 50 μL of DMPO, and then, 5 mg of Pt/P25 was dispersed in the mixture solution by ultrasonic treatment. Then, the glass capillary containing the above suspension was placed in a glass tube. The glass tube was then placed in the ESR cavity. After irradiation under a 500 W xenon lamp, the spectra were recorded.

Catalytic Testing. Photocatalytic reactions were carried out in a quartz tube reactor with an interlayer for circulating water. Typically, 5 mg of the catalyst was ultrasonically dispersed in the mixed solution (1.0 M NH_3) of 0.35 mL of ammonia aqueous solution (25 wt %) and 4.65 mL of methanol. Then, the reactor was cleaned and filled with Ar. The reaction temperature was controlled by circulating water and stirring for 30 min prior to irradiation. After the substrate reached adsorption equilibrium, the light equipment with a 500 W xenon lamp was operated for the required time. After the reaction, the liquid products were analyzed using an Agilent 7890A series gas chromatograph (GC) equipped with a DM-35 amine column and a flame ionization detector. Gaseous products, including H_2, CH_4, CO, and CO_2, were analyzed using an INFICON Micro GC Fusion equipped with a molecular sieve 5A column and a high-sensitivity thermal conductivity detector. The liquid products without ammonia were analyzed using a high-performance liquid chromatograph (Shimadzu LC-20A) equipped with a Shodex SUGAR SH-1011 column using a diluted H_2SO_4 aqueous solution as the mobile phase. For the recycling experiment, the spent catalyst was centrifuged and washed with methanol three times. Subsequently, the recovered catalyst was reused without drying using the same procedure. The yields of organic products and H_2 were quantified by the peak areas in the above chromatographs using an external standard method. The

https://doi.org/10.1021/acsomega.2c01323
ACS Omega 2022, 7, 19614−19621

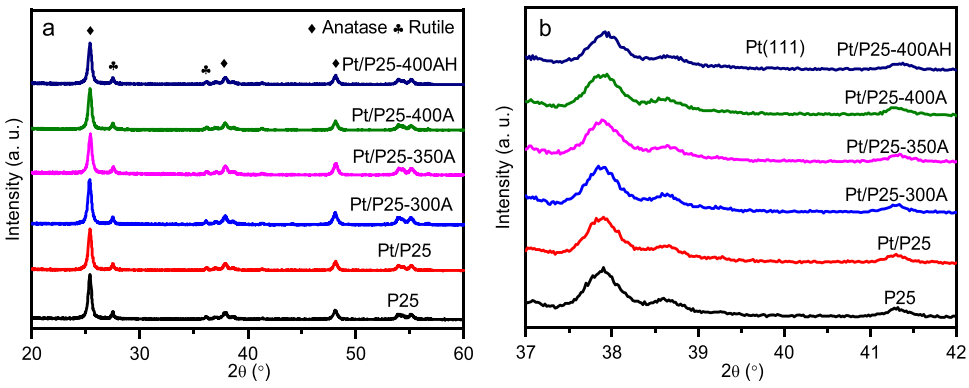

Figure 1. XRD patterns of the 0.50 wt % Pt/P25 catalyst before and after thermal treatment. (a) XRD patterns of the wide-angle range (20−60°) and (b) XRD patterns of the narrow-angle range (37−42°).

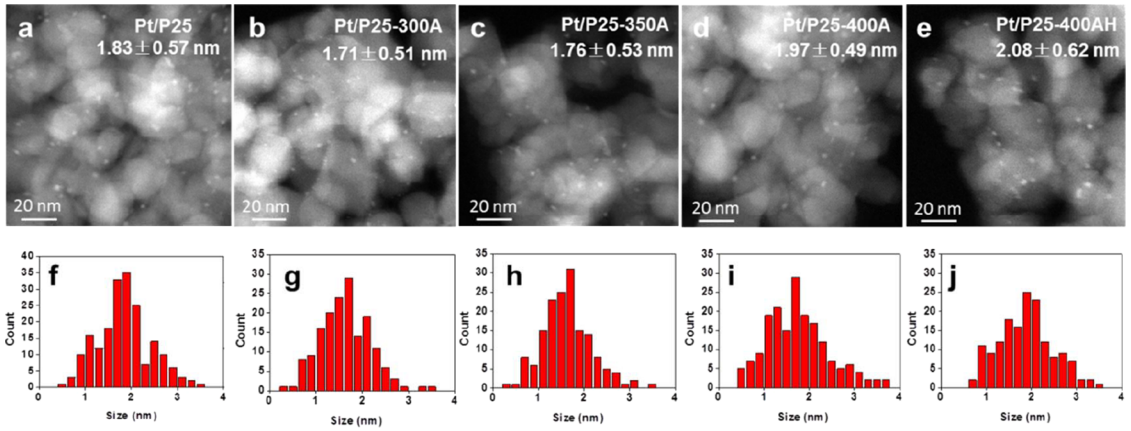

Figure 2. (a−e) STEM images and (f−j) particle size distributions of the 0.50 wt % Pt/P25 catalyst before and after thermal treatment.

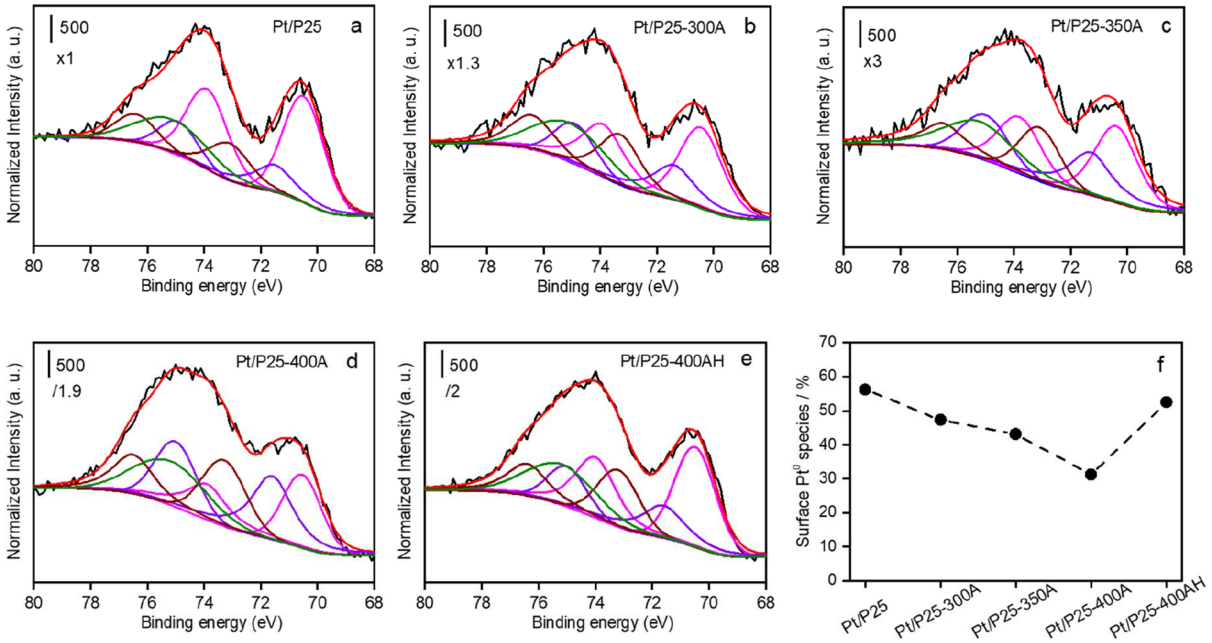

Figure 3. (a−e) Pt 4f XPS spectra and (f) evolution of the surface Pt oxidation state of the 0.50 wt % Pt/P25 catalyst before and after thermal treatment.

ratio of photogenerated electrons and holes (e^-/h^+ ratio) was estimated based on the product formation using eqs 1−3.[19]

$$CH_3OH + 2h^+ \rightarrow HCHO + 2H^+ \quad (1)$$

$$2CH_3OH + 2h^+ \rightarrow HOCH_2CH_2OH + 2H^+ \quad (2)$$

$$2H^+ + 2e^- \rightarrow H_2 \quad (3)$$

https://doi.org/10.1021/acsomega.2c01323
ACS Omega 2022, 7, 19614−19621

RESULTS AND DISCUSSION

Figure 1 shows the XRD patterns of the 0.50 wt % Pt/P25 catalyst with different treatment conditions. All the catalysts displayed similar diffraction lines, and only the crystals of anatase and rutile could be observed. No evidence of characteristic lines was found for the crystalline metallic Pt^0 or Pt oxide phase from Figure 1b, which could be ascribed to the low Pt content (approximately 0.50 wt % Pt). As shown in Figure 1 and Table S1, the relative intensity and crystallite size of the samples were nearly unchanged. Moreover, little change in the surface area was observed, with a common value of approximately 50 $m^2\ g^{-1}$.[20] The thermal treatment hardly affected the crystal structure and specific surface area of the P25 support. Similarly, the XRD patterns of Pt, Au, and Pd loaded onto TiO_2 samples with different crystallinities only showed the diffraction peaks of the corresponding TiO_2 phases due to the low metal loadings (Figure S1).

As shown in Figure S2, the size of the P25 support was approximately 20 nm, and the Pt nanoparticles (NPs) were highly dispersed in the 0.50 wt % Pt/P25 catalyst prepared by the photodeposition method. Moreover, the size of Pt NPs did not change significantly after treatment at different temperatures. Figure 2 shows the HAADF−STEM images of the 0.50 wt % Pt/P25 catalyst with different treatment conditions and the corresponding size distribution of the Pt NPs. It can be seen that that Pt species were highly dispersed in a form of clusters or ultrasmall NPs. The particle size of Pt NPs did not change significantly after either the calcination or reduction treatment. According to the STEM images, thermal treatment below a certain temperature would not significantly affect the size of Pt NPs. To further explore the effect of thermal treatment on the cocatalyst Pt on the surface of P25, the oxidation states of the Pt species were analyzed by XPS. Notably, the Pt 4f signal is overlapped with the inelastic scattering part of Ti 3s (Figure S3), which hinders the peak fitting.[21] The following procedure was adopted to resolve the Pt 4f signal from the inelastic scattering contribution of Ti 3s. The Ti 3s signals of P25 and Pt/P25 were collected, including the inelastic scattering part. The obtained curve from P25 was used to define constraints linking the Ti 3s line and its inelastic scattering part: the relative peak position and relative intensity of two parts as well as the full-width half-maximum (FWHM) were determined. During the peak fitting of Pt/P25, information on the inelastic scattering part (green line in Figure 3) was determined by the Ti 3s line. The Pt 4f line was then resolved from the inelastic scattering contribution of Ti 3s. The area ratio between Pt $4f_{7/2}$ and $4f_{5/2}$ was fixed at 4:3, and the FWHM was fixed at around 1.8. The binding energy difference between Pt $4f_{7/2}$ and $4f_{5/2}$ fixed at around 3.3 eV was used for all Pt/P25 catalysts. The detailed fitting parameters are shown in Table S2. Figure 3 indicates that Pt^0 ($4f_{7/2}$ = 70.5 eV, $4f_{5/2}$ = 73.9 eV), Pt^{2+} ($4f_{7/2}$ = 71.5 eV, $4f_{5/2}$ = 74.9 eV), and Pt^{4+} ($4f_{7/2}$ = 73.1 eV, $4f_{5/2}$ = 76.4 eV) are on the surface of the support.[22] The Pt/P25 catalyst prepared by photodeposition mainly comprised metallic Pt^0. The Pt^0 content continuously decreased with the increase in the calcination temperature, while the Pt^{2+} and Pt^{4+} contents increased. By reducing the catalyst calcined at 400 °C, the Pt^0 content can be increased to a level similar to that of the initial catalyst prepared by photodeposition (Figure 3f).

The photocatalytic behavior of different metals loaded on TiO_2 with different structures is summarized in Table 1. When the methanol−ammonia mixture solution was used as the reaction substrate, the high value-added chemical HMT was produced during the photocatalytic H_2 evolution. When bare P25 was used as the catalyst (entry 1), the formation rates of HMT and H_2 were as low as 0.15 and 0.79 mmol $g_{cat}^{-1}\ h^{-1}$, respectively. When P25 was deposited with a noble metal as a cocatalyst (entries 2−4), the catalytic performance was significantly improved. In all cases, the selectivity of HMT exceeded 99.0%, and the amount of the byproduct ethylene glycol was negligible. The photogenerated e^-/h^+ ratio was close to 1.00, indicating that HCHO was the main product accompanying H_2 according to eqs 1−3. The function of Pt was further evidenced by the photocatalytic dehydrogenation of methanol on the catalysts with and without Pt species in the absence of NH_3 (Table S3). In this case, the main liquid phase product was formaldehyde. The formation rate of formaldehyde could be significantly increased from 0.49 to 31.38 mmol $g_{cat}^{-1}\ h^{-1}$ when Pt was photodeposited onto P25 (Pt/P25). However, the performance decreased when Pt/P25 was calcined at 400 °C (Pt/P25-400A). Given the high work function of noble metals, they were deposited on the surface of the semiconductor, which is beneficial to the separation of photogenerated electrons and holes.[23] The catalyst decorated with Pt as the cocatalyst showed the highest catalytic activity, and the formation rates of HMT and H_2 reached 11.39 and 71.53 mmol $g_{cat}^{-1}\ h^{-1}$, respectively. In addition, the comparison of the catalytic activities of the different crystalline phases of TiO_2 (Pt/TiO_2-A and Pt/TiO_2-R) indicates that the Pt/P25 catalyst exhibited the best activity. This finding can be attributed to the approximate composition of P25, that is, 80% anatase and 20% rutile, which is beneficial to the separation of photogenerated carriers.[24] The catalytic activity of TiO_2, which exposed different crystal facets, was also explored (entries 7 and 8). TiO_2 samples with the (101) and (001) facets all showed the structure of anatase (Figure S1).[18] The results revealed that TiO_2 containing more (101) facets showed a higher photocatalytic activity.

Figure 4a illustrates the effect of Pt loading on the catalytic performance of Pt/P25. The formation rates of HMT and H_2 initially increased with the increase in the Pt content and reached the maximum at an approximately 0.50−1.00 wt % Pt loading. This trend can be ascribed to the cocatalyst role of Pt

Table 1. Photocatalytic Performance of Several Metals Loaded on TiO_2 with Different Structures[a]

		formation rate (mmol $g_{cat}^{-1}\ h^{-1}$)[c]		
entry	catalyst	HMT	H_2	e^-/h^+ ratio[b]
1	P25	0.15	0.79	0.89
2	Pt/P25	11.39	71.53	1.02
3	Pd/P25	5.38	38.53	1.18
4	Au/P25	2.36	18.05	1.28
5	Pt/TiO_2-A	5.45	35.47	1.09
6	Pt/TiO_2-R	1.65	11.22	1.14
7	Pt/TiO_2-101	4.21	28.22	1.12
8	Pt/TiO_2-001	2.87	19.71	1.15

[a]Reaction conditions: metal loading = 0.50 wt %; solution = 93 vol % methanol + 7 vol % ammonia aqueous solution, $C(NH_3)$ = 1 M, 5 mL; Ar atmosphere; light source = 700 mW/cm^2, λ > 300 nm; temperature = 55 °C; time = 2 h. [b]e^-/h^+ ratio = $[2 \times n(H_2) + 2 \times n(CH_4)]/[12 \times n(HMT) + 4 \times n(HCOOH) + 4 \times n(CO)]$. [c]The selectivity of HMT is >99.0%.

https://doi.org/10.1021/acsomega.2c01323
ACS Omega 2022, 7, 19614−19621

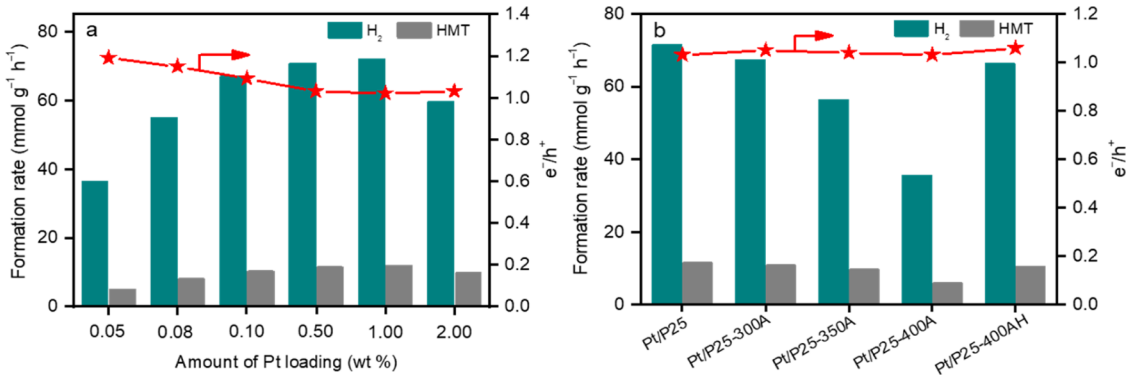

Figure 4. Comparison of photocatalytic performance of the Pt/P25 catalyst with different Pt loadings. (a) HMT and H_2 formation rates as a function of Pt loading and (b) HMT and H_2 formation rates as a function of thermal treatment. The reaction conditions are the same as Table 1.

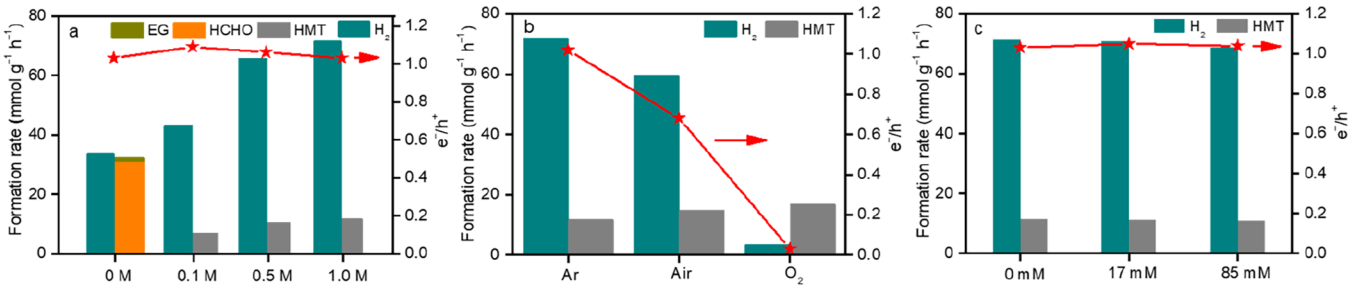

Figure 5. Photocatalytic performance of 0.50 wt % Pt/P25 under different reaction conditions. (a) Product formation rates as a function of NH_3 concentration and (b) product formation rates under different atmospheres. (c) Product formation rates as a function of Cl^- concentration. Other reaction conditions are the same as Table 1.

in capturing photogenerated electrons. However, the catalytic activity began to decrease as the Pt loading exceeded the optimal value. As shown in Figure S4, when the loading of Pt was up to 2.00 wt %, a weak and broad peak can be observed around 39.8°, corresponding to metallic platinum. The growth and agglomeration of Pt NPs were observed with the increase in the Pt content from Figure S5. According to the existing literature, a high Pt loading on the semiconductor leads to blockage of the photosensitive surface and decreases the light adsorption. Furthermore, the excessive metal deposited on the surface of the semiconductor may become the recombination center of the photogenerated electrons and holes.[25,26] The photocatalytic activity of the Pt/P25 samples subjected to different thermal treatments is shown in Figure 4b. The Pt/P25 catalyst prepared by the photodeposition method showed the best activity. As the calcination temperature in air continued to increase, the catalytic activity declined accordingly. By reducing the calcined catalyst, the catalytic activity can be essentially recovered. Given that the STEM image shown in Figure 2 indicates that thermal treatment has little effect on the particle size of the Pt NPs, the change in the valence state of Pt may be responsible for this variation in activity, and the metallic Pt NPs are a suitable cocatalyst.[27,28]

The presence of ammonia is critical to the production of HMT. As shown in Table S3 and Figure 5a, when the reaction was performed in the absence of ammonia, the main product was formaldehyde accompanied by a small amount of ethylene glycol. The selectivity of formaldehyde was approximately 93.9%, which was similar to that of methanol gas phase oxidation,[29] while ethylene glycol was obtained by the photocatalytic coupling of methanol and formaldehyde.[30] The formation rates of formaldehyde and H_2 were 31.38 and 33.37 mmol g_{cat}^{-1} h^{-1}, respectively. When ammonia was present, the product changed to HMT. Because the reaction of HMT formation through condensation of formaldehyde and ammonia can achieve over 98% completion, the inhibition of byproduct generation from methanol oxidation is an important part of the process.[31] After the addition of ammonia, the selectivity of the byproduct ethylene glycol dropped to less than 1.0% because formaldehyde underwent a condensation reaction with ammonia rather than photocatalytic coupling with methanol. Moreover, the formation rates of HMT and H_2 increased with the concentration of ammonia in the solution, indicating that the condensation of formaldehyde and ammonia was beneficial to the methanol dehydrogenation and to H_2 evolution. The effect of O_2 on the catalytic activity was also explored (Figure 5b). By replacing Ar with air and pure O_2, as the O_2 content in the reaction vessel increased, the HMT yield increased, but H_2 formation and the e^-/h^+ ratio decreased drastically. This can be ascribed to the consumption of H_2 from methanol dehydrogenation by O_2. Under a pure O_2 atmosphere, almost no H_2 was detected, but the HMT yield did not increase significantly, which may be because too much O_2 will lead to excessive oxidation of formaldehyde to form deep oxidation products such as formic acid and CO_2. Furthermore, we studied the effect of Cl^- ions on the performance by adding NaCl to the reaction system (Figure 5c). It can be seen that the catalytic activity hardly changed with the concentration of Cl^- ions in the reaction system. This finding shows that the Pt/P25 activity is not affected by the residual Cl^- ions.

The in situ ESR spectrum is used to detect the generation of radicals. Figure 6 shows the ESR spectrum of Pt/P25 using DMPO as the spin-trapping agent. When the suspension was

https://doi.org/10.1021/acsomega.2c01323
ACS Omega 2022, 7, 19614−19621

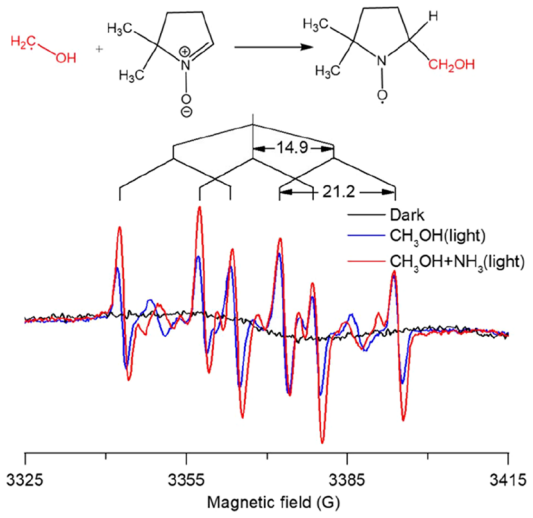

Figure 6. In situ ESR spectra for the systems containing the 0.50 wt % Pt/P25 catalyst in CH_3OH and CH_3OH/NH_3 aqueous solutions.

tested under radiation, the radical signal can be ascribed to the generation of a hydroxymethyl radical ($\cdot CH_2OH$) in the photocatalytic reaction system.[32] The $\cdot CH_2OH$ radical should be an intermediate for the formation of formaldehyde HCHO *via* the C−H activation of CH_3OH. A stronger signal of the $\cdot CH_2OH$ radical was observed in methanol solution containing ammonia, indicating that the presence of ammonia promotes the generation of the $\cdot CH_2OH$ radical, which is ascribed to basic conditions favoring the adsorption of the substrate on the catalyst surface. In the photocatalytic dehydrogenation of CH_3OH, CH_3OH was first oxidized to $\cdot CH_2OH$ by the photogenerated holes and then further dehydrogenated to HCHO to participate in the follow-up reactions. Table S4 illustrates the direct condensation of HCHO with NH_3 without radiation. Although the concentration of HCHO was only 0.70 mmol, which is much lower than the concentration of methanol during photocatalysis (14.0 mmol/mL), most HCHO was consumed within 0.2 h (the conversion is >95% based on the amount of the product HMT). The consumption rate of formaldehyde through the condensation with ammonia without a catalyst was approximately 690.00 mmol g_{cat}^{-1} h^{-1} (Table S4), which was much higher than the formation rate of formaldehyde (31.38 mmol g_{cat}^{-1} h^{-1}) by the dehydrogenation of methanol on the Pt/P25 catalyst (Table S3). The rapid condensation of formaldehyde with ammonia in the absence of a catalyst indicates that the process is spontaneous and the contributions of Pt/P25 to the condensation are minor.

The UV−vis absorbance spectra (Figure S6a) show that bare P25 exhibits UV absorption at wavelengths shorter than 390 nm. The loading of Pt can obviously enhance the absorption at the visible-light range owing to the localized surface plasma resonance effect of the Pt NPs.[33] The corresponding values of the band gap were determined by the Tauc plot (Figure S6b). The band gap of bare P25 was 3.35 eV, and those of Pt/P25 catalysts treated with different temperatures were around 3.24−3.32 eV. The addition of Pt enhanced the wavelength range of light absorption but had no significant changes on the band gap.

To investigate the durability of Pt/P25, we performed the photocatalytic reaction by prolonging the reaction time and reusing the catalyst (Figure 7). The results showed that the formation rates of HMT and H_2 linearly increased as a function of reaction time, indicating that the catalyst structure and performance were stable (Figure 7a). In addition, after five cycles, no significant deactivation of the photocatalytic performance was seen, and the formation rates of HMT and H_2 in each run were approximately 10.99 and 68.83 mmol g_{cat}^{-1} h^{-1}, respectively (Figure 7b). As shown in Figures S7 and S8, the size of Pt NPs in used Pt/P25 slightly increased from 1.83 to 2.35 nm, while the valence state of Pt was still dominated by metallic Pt^0 (52.8%). The findings indicate that the structure of Pt/P25 can be essentially stable during the photocatalytic operations.

Figure 8 depicts the possible conversion mechanism of methanol and ammonia to HMT and H_2 under irradiation. Methanol is first dehydrogenated into $\cdot CH_2OH$ and H^+ ions by the photogenerated holes, and $\cdot CH_2OH$ radicals are easily and further dehydrogenated to form formaldehyde (HCHO). The H^+ ion is generated by the two-step dehydrogenation transfer to the surface of the Pt NPs and reduced by the electrons from the conduction band to release H_2. The obtained HCHO reacts with ammonia in the solution and undergoes dehydration and condensation to produce HMT.

CONCLUSIONS

We have demonstrated light-driven methanol dehydrogenation coupled with the condensation of formaldehyde with ammonia to produce H_2 and HMT in one step by using the Pt-modified semiconductor nanophotocatalyst Pt/P25. This reaction follows a tandem process in which methanol is oxidatively

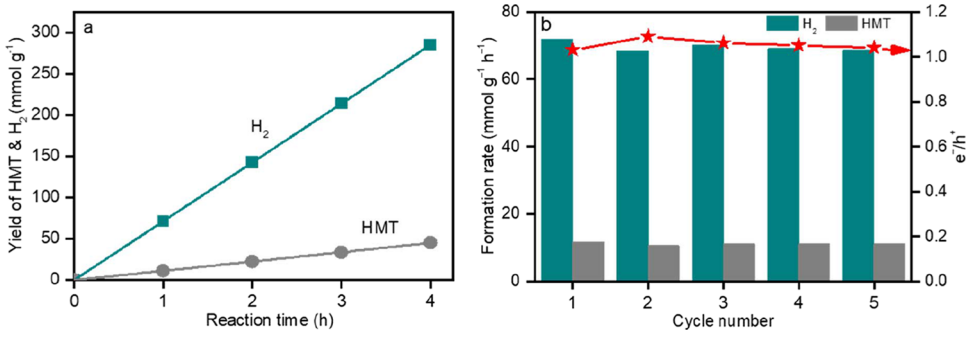

Figure 7. Photocatalytic performance of the 0.50 wt % Pt/P25 catalyst as a function of the reaction time and recycle number. (a) HMT and H_2 formation rates as a function of reaction time and (b) HMT and H_2 formation rates as a function of the recycle number. Reaction conditions are the same as Table 1.

https://doi.org/10.1021/acsomega.2c01323
ACS Omega 2022, 7, 19614−19621

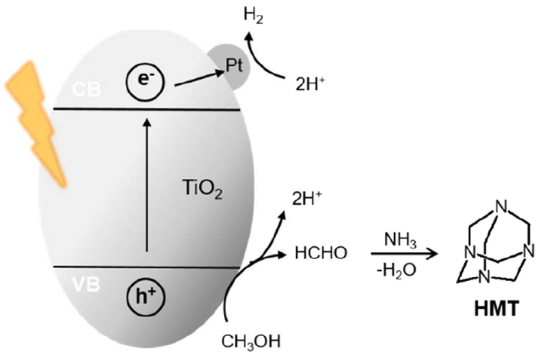

Figure 8. Proposed mechanism for the photocatalytic methanol dehydrogenation followed by condensation with NH_3 to produce HMT and H_2 over Pt/P25.

dehydrogenated to H_2 and formaldehyde by photogenerated holes and formaldehyde immediately reacts with ammonia in the solution to produce HMT through dehydration and condensation. Increasing the ammonia concentration can effectively accelerate this process. The hydroxymethyl radical ($\cdot CH_2OH$) is an important intermediate in this photocatalytic process. This work provides a green path to effectively couple photocatalytic H_2 evolution with fine chemical synthesis through the full utilization of photogenerated electrons and holes.

■ ASSOCIATED CONTENT

Supporting Information

The Supporting Information is available free of charge at https://pubs.acs.org/doi/10.1021/acsomega.2c01323.

XRD patterns of several TiO_2-supported catalysts; STEM images of Pt/P25 with different Pt contents; TEM images, UV−vis spectra, and structural properties of the 0.50 wt % Pt/P25 catalyst with different thermal treatments; photocatalytic dehydrogenation of methanol without NH_3; reaction between formaldehyde and ammonia; TEM image, HAADF−STEM image, and Pt 4f XPS profile of the used 0.50 wt % Pt/P25 catalyst (PDF)

■ AUTHOR INFORMATION

Corresponding Author

Youzhu Yuan − *State Key Laboratory of Physical Chemistry of Solid Surfaces, National Engineering Laboratory for Green Chemical Productions of Alcohols−Ethers−Esters, College of Chemistry and Chemical Engineering, Xiamen University, Xiamen 361005, China*; orcid.org/0000-0003-1668-9984; Email: yzyuan@xmu.edu.cn

Authors

Weikun Chen − *State Key Laboratory of Physical Chemistry of Solid Surfaces, National Engineering Laboratory for Green Chemical Productions of Alcohols−Ethers−Esters, College of Chemistry and Chemical Engineering, Xiamen University, Xiamen 361005, China*

Xiaoying Liu − *State Key Laboratory of Physical Chemistry of Solid Surfaces, National Engineering Laboratory for Green Chemical Productions of Alcohols−Ethers−Esters, College of Chemistry and Chemical Engineering, Xiamen University, Xiamen 361005, China*

Hui Zheng − *State Key Laboratory of Physical Chemistry of Solid Surfaces, National Engineering Laboratory for Green Chemical Productions of Alcohols−Ethers−Esters, College of Chemistry and Chemical Engineering, Xiamen University, Xiamen 361005, China*

Xiao Fu − *State Key Laboratory of Physical Chemistry of Solid Surfaces, National Engineering Laboratory for Green Chemical Productions of Alcohols−Ethers−Esters, College of Chemistry and Chemical Engineering, Xiamen University, Xiamen 361005, China*

Complete contact information is available at: https://pubs.acs.org/10.1021/acsomega.2c01323

Notes

The authors declare no competing financial interest.

■ ACKNOWLEDGMENTS

We appreciate financial support from the National Key Research and Development Program of China (2017YFA0206801), the National Natural Science Foundation of China (21972113), and the Program for Innovative Research Team in Chinese Universities (IRT_14R31).

■ REFERENCES

(1) Wang, H.; Gao, X.; Lv, Z.; Abdelilah, T.; Lei, A. Recent advances in oxidative R^1-H/R^2-H cross-coupling with hydrogen evolution via photo−/electrochemistry. *Chem. Rev.* **2019**, *119*, 6769−6787.

(2) Du, C.; Mo, J.; Li, H. Renewable hydrogen production by alcohols reforming using plasma and plasma-catalytic technologies: Challenges and opportunities. *Chem. Rev.* **2015**, *115*, 1503−1542.

(3) Zielinska, B.; Borowiakpalen, E.; Kalenczuk, R. Photocatalytic hydrogen generation over alkaline-earth titanates in the presence of electron donors. *Int. J. Hydrogen Energy* **2008**, *33*, 1797−1802.

(4) Strataki, N.; Bekiari, V.; Kondarides, D. I.; Lianos, P. Hydrogen production by photocatalytic alcohol reforming employing highly efficient nanocrystalline titania films. *Appl. Catal., B* **2007**, *77*, 184−189.

(5) Daskalaki, V. M.; Kondarides, D. I. Efficient production of hydrogen by photo-induced reforming of glycerol at ambient conditions. *Catal. Today* **2009**, *144*, 75−80.

(6) Zhang, Z.; Wang, M.; Zhou, H.; Wang, F. Surface sulfate ion on CdS catalyst enhances syngas generation from biopolyols. *J. Am. Chem. Soc.* **2021**, *143*, 6533−6541.

(7) Chai, Z.; Zeng, T.-T.; Li, Q.; Lu, L.-Q.; Xiao, W.-J.; Xu, D. Efficient visible light-driven splitting of alcohols into hydrogen and corresponding carbonyl compounds over a Ni-modified CdS photocatalyst. *J. Am. Chem. Soc.* **2016**, *138*, 10128−10131.

(8) Zhang, H.; Zhu, Z.; Wu, Y.; Zhao, T.; Li, L. TiO_2-photocatalytic acceptorless dehydrogenation coupling of primary alkyl alcohols into acetals. *Green Chem.* **2014**, *16*, 4076−4080.

(9) Xia, B.; Zhang, Y.; Shi, B.; Ran, J.; Davey, K.; Qiao, S. Z. Photocatalysts for hydrogen evolution coupled with production of value-added chemicals. *Small Methods* **2020**, *4*, 2000063.

(10) Qi, M. Y.; Conte, M.; Anpo, M.; Tang, Z. R.; Xu, Y. J. Cooperative coupling of oxidative organic synthesis and hydrogen production over semiconductor-based photocatalysts. *Chem. Rev.* **2021**, *121*, 13051−13085.

(11) Chao, Y.; Lai, J.; Yang, Y.; Zhou, P.; Zhang, Y.; Mu, Z.; Li, S.; Zheng, J.; Zhu, Z.; Tan, Y. Visible light-driven methanol dehydrogenation and conversion into 1,1-dimethoxymethane over a non-noble metal photocatalyst under acidic conditions. *Catal. Sci. Technol.* **2018**, *8*, 3372−3378.

(12) Li, J.-Y.; Li, Y.-H.; Zhang, F.; Tang, Z.-R.; Xu, Y.-J. Visible-light-driven integrated organic synthesis and hydrogen evolution over 1D/2D CdS-$Ti_3C_2T_x$ MXene composites. *Appl. Catal., B* **2020**, *269*, No. 118783.

(13) Zhang, H.; Xie, S.; Hu, J.; Wu, X.; Zhang, Q.; Cheng, J.; Wang, Y. C-H activations of methanol and ethanol and C-C couplings into diols by zinc-indium-sulfide under visible light. *Chem. Commun.* **2020**, *56*, 1776−1779.
(14) Dreyfors, J. M.; Jones, S. B.; Sayed, Y. Hexamethylenetetramine: a review. *Am. Ind. Hyg. Assoc. J. (1958-1999)* **1989**, *50*, 579−585.
(15) Kirillov, A. M. Hexamethylenetetramine: An old new building block for design of coordination polymers. *Coord. Chem. Rev.* **2011**, *255*, 1603−1622.
(16) Andersson, A.; Holmberg, J.; Häggblad, R. Process improvements in methanol oxidation to formaldehyde: Application and catalyst development. *Top. Catal.* **2016**, *59*, 1589−1599.
(17) Tian, C.; Fang, H.; Chen, H.; Chen, W.; Zhou, S.; Duan, X.; Liu, X.; Yuan, Y. Photodeposition of Pd onto TiO_2 nanowires for aqueous-phase selective hydrogenation of phenolics to cyclohexanones. *Nanoscale* **2020**, *12*, 2603−2612.
(18) Fu, C.; Li, F.; Zhang, J.; Li, D.; Qian, K.; Liu, Y.; Tang, J.; Fan, F.; Zhang, Q.; Gong, X.-Q.; Huang, W. Site sensitivity of interfacial charge transfer and photocatalytic efficiency in photocatalysis: Methanol oxidation on anatase TiO_2 nanocrystals. *Angew. Chem., Int. Ed.* **2021**, *60*, 6160−6169.
(19) Xie, S.; Shen, Z.; Deng, J.; Guo, P.; Zhang, Q.; Zhang, H.; Ma, C.; Jiang, Z.; Cheng, J.; Deng, D.; Wang, Y. Visible light-driven C−H activation and C−C coupling of methanol into ethylene glycol. *Nat. Commun.* **2018**, *9*, 1181.
(20) Jiang, Z.; Zhang, Z.; Shangguan, W.; Isaacs, M. A.; Durndell, L. J.; Parlett, C. M. A.; Lee, A. F. Photodeposition as a facile route to tunable Pt photocatalysts for hydrogen production: on the role of methanol. *Catal. Sci. Technol.* **2016**, *6*, 81−88.
(21) Batalović, K.; Bundaleski, N.; Radaković, J.; Abazović, N.; Mitrić, M.; Silva, R. A.; Savić, M.; Belóević-Čavor, J.; Rakočević, Z.; Rangel, C. M. Modification of N-doped TiO_2 photocatalysts using noble metals (Pt, Pd) − a combined XPS and DFT study. *Phys. Chem. Chem. Phys.* **2017**, *19*, 7062−7071.
(22) Li, N.; Chen, Q.-Y.; Luo, L.-F.; Huang, W.-X.; Luo, M.-F.; Hu, G.-S.; Lu, J.-Q. Kinetic study and the effect of particle size on low temperature CO oxidation over Pt/TiO_2 catalysts. *Appl. Catal., B* **2013**, *142-143*, 523−532.
(23) Ismail, A. A.; Al-Sayari, S. A.; Bahnemann, D. W. Photodeposition of precious metals onto mesoporous TiO_2 nanocrystals with enhanced their photocatalytic activity for methanol oxidation. *Catal. Today* **2013**, *209*, 2−7.
(24) Zhang, J.; Xu, Q.; Feng, Z.; Li, M.; Li, C. Importance of the relationship between surface phases and photocatalytic activity of TiO_2. *Angew. Chem., Int. Ed.* **2008**, *120*, 1790−1793.
(25) Gratian, R.; Bamwenda l, S. T.; Nakamura, T.; Haruta, M. Photoassisted hydrogen production from a water-ethanol solution: a comparison of activities of $Au-TiO_2$ and $Pt-TiO_2$. *J. Photochem. Photobiol., A* **1995**, *89*, 177−189.
(26) Korzhak, A. V.; Ermokhina, N. I.; Stroyuk, A. L.; Bukhtiyarov, V. K.; Raevskaya, A. E.; Litvin, V. I.; Kuchmiy, S. Y.; Ilyin, V. G.; Manorik, P. A. Photocatalytic hydrogen evolution over mesoporous TiO_2/metal nanocomposites. *J. Photochem. Photobiol., A* **2008**, *198*, 126−134.
(27) Cho, Y.; Park, B.; Padhi, D. K.; Ibrahim, I. A. M.; Kim, S.; Kim, K. H.; Lee, K. S.; Lee, C. L.; Han, J. W.; Oh, S. H.; Park, J. H. Disordered-layer-mediated reverse metal-oxide interactions for enhanced photocatalytic water splitting. *Nano Lett.* **2021**, *21*, 5247−5253.
(28) Jiang, Z.; Qi, R.; Huang, Z.; Shangguan, W.; Wong, R. J.; Lee, A. Impact of methanol photomediated surface defects on photocatalytic H_2 production over Pt/TiO_2. *Energy Environ. Mater.* **2020**, *3*, 202−208.
(29) Haggblad, R.; Wagner, J.; Hansen, S.; Andersson, A. Oxidation of methanol to formaldehyde over a series of $Fe_{1-x}Al_x$-V-oxide catalysts. *J. Catal.* **2008**, *258*, 345−355.
(30) Fan, Y.; Bao, J.; Shi, L.; Li, S.; Lu, Y.; Liu, H.; Wang, H.; Zhong, L.; Sun, Y. Photocatalytic coupling of methanol and formaldehyde into ethylene glycol with high atomic efficiency. *Catal. Lett.* **2018**, *148*, 2274−2282.
(31) Meissner, F.; Schwiedessen, E.; Othmer, D. F. Continuous production of hexamethylenetetramine. *Ind. Eng. Chem.* **1954**, *46*, 724−727.
(32) Karimi Estahbanati, M. R.; Mahinpey, N.; Feilizadeh, M.; Attar, F.; Iliuta, M. C. Kinetic study of the effects of pH on the photocatalytic hydrogen production from alcohols. *Int. J. Hydrogen Energy* **2019**, *44*, 32030−32041.
(33) Banerjee, B.; Amoli, V.; Maurya, A.; Sinha, A. K.; Bhaumik, A. Green synthesis of Pt-doped TiO_2 nanocrystals with exposed (001) facets and mesoscopic void space for photo-splitting of water under solar irradiation. *Nanoscale* **2015**, *7*, 10504−10512.

https://doi.org/10.1021/acsomega.2c01323
ACS Omega 2022, 7, 19614−19621